# Inter- and intra-configurational transitions of europium (II) in $Ba_2Mg_3F_{10}$



2005 J. Phys.: Condens. Matter 17 1861

(http://iopscience.iop.org/0953-8984/17/12/010)

INSTITUTE OF PHYSICS PUBLISHING JOURNAL OF PHYSICS: CONDENSED MATTER

J. Phys.: Condens. Matter **17** (2005) 1861–1868 doi:10.1088/0953-8984/17/12/010

# Inter- and intra-configurational transitions of europium (II) in $Ba_2Mg_3F_{10}$

**J M Rey[1,2], J R G Thorne[2], R G Denning[2] and H Bill[1]**

[1] Département de Chimie Physique, Université de Genève, Sciences II, 30 quai E Ansermet, 1211 Genève 4, Switzerland
[2] Department of Chemistry, University of Oxford, Inorganic Chemistry Laboratory, South Parks Road, Oxford OX1 3QR, UK

Received 19 January 2005
Published 11 March 2005
Online at stacks.iop.org/JPhysCM/17/1861

**Abstract**

An optical investigation of the properties of europium (II) ions introduced in $Ba_2Mg_3F_{10}$ single crystals is presented. The spectra and time-dependence of both the inter-configurational (f–d) and the intra-configurational (f–f) transitions are described. The emission spectrum consists of two emitting $Eu^{2+}$ centres, each showing one broad f–d band and one $^6P_{7/2}$ quartet. The thermal equilibrium between the f–f and f–d emitting states is investigated and found to take place on a microsecond timescale for one of the two $Eu^{2+}$ centres. The spectroscopic results combined with numerical modelling of the influence of the host crystal on the $^6P_{7/2}$ energy scheme allow the assignment of each f–f and f–d emission to its corresponding $Eu^{2+}$ centre.

## 1. Introduction

The binary and ternary alkaline earth fluorides and fluoro-halides form a number of crystal structure types, with symmetry ranging from cubic to monoclinic. Due to their large electronic bandgaps, they are transparent to visible and UV radiation and often to wavelengths in the vacuum UV region. Most compounds easily accommodate rare earth impurity ions (REI). For these reasons they are potentially promising systems as laser host crystals [1, 2], or when optical information storage and signal processing applications are envisioned [3, 4]. In parallel, there are basic aspects of interest regarding these systems which arise from the variety of local environments for the REI observed throughout these structures. For example, divalent europium ions introduced in different members of the matlockite series MFX (M = Ca, Sr, Ba and X = Cl, Br) experience only small differences in their local environment, but the ligand field acting on the ground state of $Eu^{2+}$ ions varies strongly along the MFX series [5]. The combined effect of the symmetry, the geometry and the number of coordinating anions shows up strikingly when the optical emission spectra of $Eu^{2+}$ in different crystal structures are compared [6, 7].

  

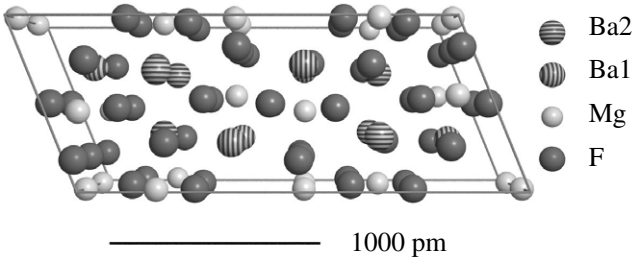


**Figure 1.** Unit cell of the $Ba_2Mg_3F_{10}$ crystal structure; the a crystal axis is horizontal and the *b* axis perpendicular to the page.

The inter-configurational $4f^n$–$4f^{n-1}5d^1$ (f–d) transitions in lanthanide ions are of great interest, especially for lamp and display applications [8]. For trivalent lanthanides, the f–d transitions generally lie in the vacuum UV region [9–11]. These f–d transitions are observed at lower energy for ions with lower electron affinity like $Eu^{2+}$. Depending on the host crystal, the $Eu^{2+}$ f–d emitting band can occur in any region of the spectrum from the UV to the infrared [7]. Compared to the intra-configurational (f–f) transitions, the f–d energies are more dependent on the host crystal since the 5d orbitals have a greater radial extension and are more sensitive to the crystal field.

This paper presents an investigation of the inter- and intra-configurational transitions of europium ions introduced in $Ba_2Mg_3F_{10}$ single crystals. The title compound is monoclinic with space group $C2/m$ (no. 12) [12]. Figure 1 presents the $Ba_2Mg_3F_{10}$ crystal structure; there are two different $Ba^{2+}$ sites and both have $C_s(m)$ site symmetry. A previous electron paramagnetic resonance (EPR) investigation of europium doped $Ba_2Mg_3F_{10}$ single crystals has shown that the $Eu^{2+}$ impurity occupies both barium lattice sites [13]. In this paper we present luminescence data for $Eu^{2+}$ ions in the $Ba_2Mg_3F_{10}$ host. The spectra and time-dependence of both the inter-configurational (f–d) and the intra-configurational (f–f) transitions are shown. The exchange of population between the $4f^7$ and $4f^65d^1$ configuration is also discussed. The spectroscopic results combined with numerical modelling of the influence of the host crystal on the $4f^7$ energy scheme allow the assignment of each f–f and f–d emission to its corresponding $Eu^{2+}$ centre.

## 2. Experimental details

Single crystals of $Ba_2Mg_3F_{10}$ were grown by slowly cooling a stoichiometric mixture of the fluorides $BaF_2$ (Merck, Suprapur) and $MgF_2$ (Balzers, oxygen-free, vacuum deposition grade) in a carbon crucible under a controlled atmosphere of typically 0.2 bar (Ar 57) in a high vacuum furnace. The pressure was stabilized with the aid of a cold finger (liquid nitrogen cooled) attached to the furnace. Great care was taken to avoid oxygen contamination during growth. $Ba_{2-x}Mg_3F_{10}$:$Eu_x^{2+}$ crystals, nominally $x = 0.002$, were used for the optical experiments.

Continuous wave (CW) optical measurements were carried out with two home-built spectrophotometers already described elsewhere [13, 14]. Time resolved measurements were performed with the aid of two different set-ups. The first used a nitrogen laser as excitation source (KX2, Oxford Laser, pulse length $< 20$ ns, wavelength 337.1 nm, repetition rate 1 Hz). The emission was analysed with a Cary14 monochromator and two types of detector were used, a photodiode (Hamamatsu S3883) and a photomultiplier (Hamamatsu H6240-01). The signals were collected and averaged with a digital oscilloscope (LeCroy 9420). The fourth

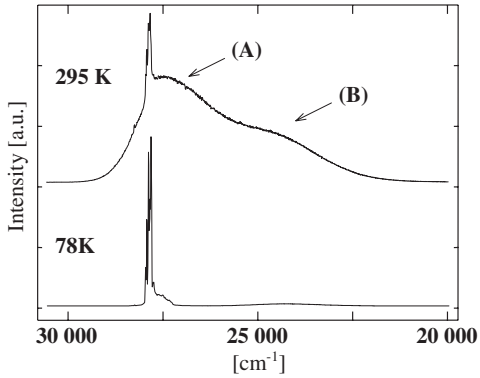


**Figure 2.** Emission spectra of $Ba_2Mg_3F_{10}$:Eu(0.2%) single crystal at 295 and 78 K with continuous-wave excitation at 33 300 $cm^{-1}$. The (A) and (B) labels indicate the two observed f–d emission bands.

harmonic (266 nm) of a pulsed Nd:YAG laser (SL803, Spectron) was used in the second set-up. The repetition rate was 10 Hz and the pulse width 15 ns. The emission was analysed with a monochromator (Spex 1404) and detected with a photomultiplier (EMI 9813QB), followed either by a photon-counting unit (SR400, Stanford Research) or a digital oscilloscope (Hewlett Packard 54111D).

## 3. Results and discussion

### *3.1. Continuous wave optical spectra*

Low resolution emission spectra, recorded at 295 and 78 K, are shown in figure 2. The 295 K spectrum is dominated by two broad $4f^65d^1$–$4f^7$ emission bands (maxima at 27 700 $cm^{-1}$ (A) and 24 600 $cm^{-1}$ (B)) of nearly Gaussian spectral profile, and a $4f^7$–$4f^7$ intra-configurational multiplet centred at 27 800 $cm^{-1}$. The f–f emission intensity is clearly increased at the expense of the f–d emission when the temperature is lowered. The electronic origin of the lowest $4f^65d^1$ state is thus at higher energy than the first excited state ($^6P_{7/2}$) of the $4f^7$ configuration.

The 78 K emission spectrum recorded at higher resolution shows that the f–f energy level manifold is comprised of eight components (figure 3). Because the relative intensity of these lines depends upon the excitation wavelength, they can be separated into two groups of four lines given in table 1 and arbitrarily labelled (a) and (b) in figure 3. Each quartet is identified as the $^6P_{7/2}$–$^8S_{7/2}$ transition set due to one of the two types of $Eu^{2+}$ centre present in the structure. Each $Eu^{2+}$ centre generates four emitting lines since the $^6P_{7/2}$ state is split into four components by the ligand-field of $C_s$ point symmetry.

### *3.2. Numerical modelling of the $^6P_{7/2}$ energy scheme*

Calculations utilize the F-shell package of Professor M F Reid (University of Canterbury, New Zealand), and free ion parameters for $Eu^{2+}$ taken from [15] give a good approximation to the absolute energy of $^6P_{7/2}$. The ligand field calculation uses a single scaling parameter $\langle r^2 \rangle = 0.28$ Å$^2$ to determine the second rank crystal field parameters, $B_2^k$ with $k = 0, 1, 2$. Although fourth and sixth order parameters are also included in the calculation, they have no effect on the splitting of S and P component states (only on the absolute energies of the levels themselves).

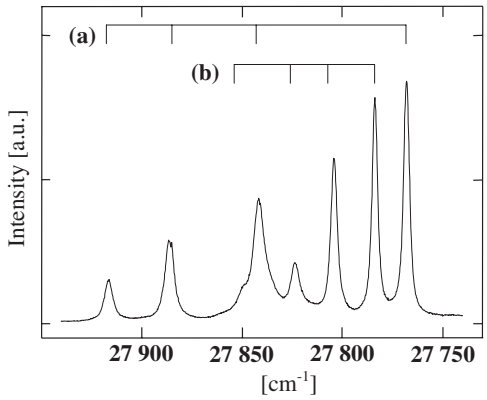


**Figure 3.** $4f^7$–$4f^7$ intra-configurational emission spectrum of $Ba_2Mg_3F_{10}$:Eu (0.2%) single crystal at 78 K with continuous wave excitation at 33 300 $cm^{-1}$. The (a) and (b) labels indicate the two groups of four ligand field components for each $Eu^{2+}$ centre.

**Table 1.** Experimental positions and lifetimes of the different f–d and f–f emissions in $Ba_2Mg_3F_{10}$:$Eu^{2+}$.

| | | Positions ($cm^{-1}$) | Lifetime ($\mu$s) | | Positions ($cm^{-1}$) | Lifetime ($\mu$s) |
|---|---|---|---|---|---|---|
| 295 K | f–d (A) | Maximum at 27 500 | 43 | f–d (B) | Maximum at 24 500 | 27 |
| 78 K | f–f (a) | 27 768<br>27 841<br>27 886<br>27 916 | 1752 | f–f (b) | 27 784<br>27 804<br>27 823<br>27 849 | 705 |

A convenient measure of the experimental and calculated effective crystal field within each (quartet) multiplet is the splitting parameter $\sigma$, defined as the square root of the second moment of the energies of the ($n = 4$) components, i.e.

$$\sigma^2 = \frac{1}{n}\sum_n (E_n - \bar{E})^2 \tag{1}$$

where $\bar{E}$ is the mean energy of the components.

We have performed the calculations of $\sigma$ including all ligand-field ions within a radius from 600 pm from the impurity $Eu^{2+}$ ion, up to a radius of 920 pm. The results are shown in figure 4 from which it is clear that reasonable energy level convergence in the calculation has occurred at this upper distance from the impurity. (The lines are guides to the eye only.) The experimental values for the splitting parameter for both $Eu^{2+}$ sites are also shown in the figure.

The calculation leads to the $^6P_{7/2}$ ligand field components for Eu1 ($Eu^{2+}$ at a Ba1 lattice site) and for Eu2 ($Eu^{2+}$ at a Ba2 lattice site). Table 2 presents the calculated and experimental ligand-field splitting and shows that the Eu1 has a crystal-field splitting more than twice that of the Eu2 site. On the basis of table 2, we conclude that the Eu f–f(a) emissions emanate from the $Eu^{2+}$ impurity site designated Eu1 having large crystal field splitting, and the f–f(b) emissions emanate from the site designated Eu2. The small difference between the experimental and calculated ligand-field splittings could easily be explained by the $Eu^{2+}$–$Ba^{2+}$ substitution, since a small shift of $Eu^{2+}$ with respect to the $Ba^{2+}$ site is expected [16].

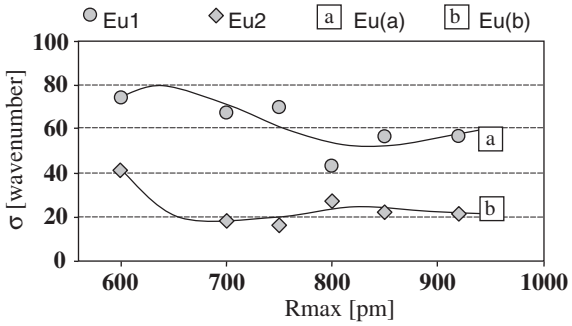


**Figure 4.** Calculated (Eu1, Eu2) and experimental (Eu(a), Eu(b)) ligand field splitting parameter $\sigma$, defined as the square root of the second moment of the components energies. For both $Eu^{2+}$ types (i.e. $Eu^{2+}$ at a Ba1 or Ba2 site in the crystal structure), the calculation of $\sigma$ has been performed including all ligand-field ions within a radius from 600 pm from the impurity $Eu^{2+}$ ion, up to a radius of 920 pm. The lines are guides to the eye only.

**Table 2.** Experimental and calculated $^6P_{7/2}$ ligand-field splittings for the two types of $Eu^{2+}$ site. The experimental splitting values come from the 78 K fluorescence data (figure 3). Eu1 and Eu2 refer, respectively, to the calculated splitting for $Eu^{2+}$ at Ba1 and Ba2 lattice sites of the $Ba_2Mg_3F_{10}$ crystal structure (figure 1).

| | Experimental | | Calculated | |
|---|---|---|---|---|
| | Eu f–f (a) | Eu f–f (b) | Eu1 | Eu2 |
| $^6P_{7/2}$ splitting | −63 | −34 | −61 | −34 |
| ($cm^{-1}$) | −33 | −8 | −38 | −4 |
| | 12 | 11 | 11 | 15 |
| | 85 | 31 | 88 | 23 |
| $\sigma$ | 56 | 24 | 57 | 22 |

### *3.3. Lifetime measurements*

The decay profiles of all the f–f and f–d emissions were measured between 78 and 295 K to determine their lifetimes as a function of temperature. The experimental uncertainty attached to these results is smaller than 5%. The results are presented in figure 5, the symbols (○) and (□) correspond to the f–f and f–d experimental lifetimes, respectively. At a given temperature each line belonging to a given f–f quartet (i.e. (a) or (b)) has the same lifetime within experimental uncertainty, confirming the previous assignment of the eight f–f lines into the quartets (a) and (b). Figure 5 also illustrates close agreement between the measured lifetimes for the f–f (a) quartet and the f–d (A) band. This shows that there is a rapid equilibrium between the emitting states corresponding to the f–f (a) and f–d (A) transitions, and indicates that both states belong to the same $Eu^{2+}$ ions. The agreement is slightly less good for the f–f (b) and f–d (B) lifetimes. Nevertheless, this result allows the association of the corresponding f–d and f–f-transitions presented in table 1.

The temperature dependences of the decay time for the two types of $Eu^{2+}$ were fitted to a three-level model to get an estimate of the energy difference ($\Delta E$) between the lowest $^6P_{7/2}$ component and the lowest $4f^65d^1$ state. Due to their close agreement, both the f–f and f–d decay times for each $Eu^{2+}$ type were all fitted together. The three-level model [17] assumes that both states have the same degeneracy and that the two emitting states are in mutual thermal equilibrium before the emission starts. Under these assumptions, the observed lifetime $\tau_{obs}$ is

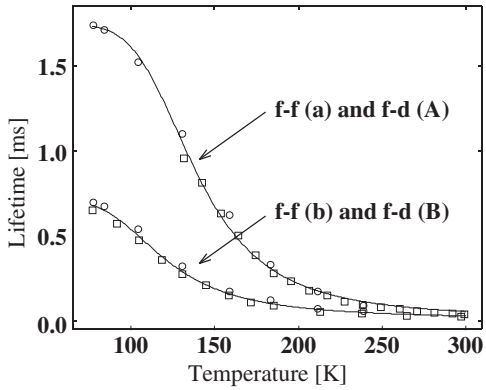


**Figure 5.** Experimental temperature evolution of the f–f (○) and f–d (□) lifetimes for the two $Eu^{2+}$ sites in $Ba_2Mg_3F_{10}$:Eu (0.2%). The curve represents the result of the simulation (see text).

**Table 3.** Parameters used to fit equation (2) to the observed emission decay for both $Eu^{2+}$ types in the $Ba_2Mg_3F_{10}$:Eu compound. The resulting f–d Stokes-shift is also given.

| | | Eu2 | | Eu1 | |
|---|---|---|---|---|---|
| Intrinsic f–f radiation lifetime, $\tau_1$ | ($\mu$s) | f–f (a) | 1740 | f–f (b) | 715 |
| Intrinsic f–d radiation lifetime, $\tau_2$ | ($\mu$s) | f–d (A) | 3 | f–d (B) | 4 |
| Energy difference, $\Delta E$ | ($cm^{-1}$) | 600 | | 450 | |
| f–d Stokes-shift | ($cm^{-1}$) | 1700 | | 7500 | |

given by:

$$\tau_{\text{obs}} = \frac{\frac{1}{\tau_1} + \frac{1}{\tau_2}\exp(\frac{-\Delta E}{k_B T})}{1 + \exp(\frac{-\Delta E}{k_B T})}. \tag{2}$$

Here $\tau_1$ and $\tau_2$ are the intrinsic radiative lifetimes of the f–f and f–d transitions, respectively. The temperature is represented by $T$ and the Boltzmann constant by $k_B$. The best fit to equation (2), shown in figure 5, is obtained with the parameters given in table 3. The obtained fitted values give reasonable estimates of the energy difference $\Delta E$, even though the variation of the intrinsic lifetime of the f–f transition ($\tau_1$) with temperature [18] and the influence of other $4f^7$ levels (e.g. $^6P_{5/2}$, $^6P_{3/2}$) [19] have not been taken into account in the above model.

At low temperature the f–d (B) decay profile has two components. Figure 6 presents this decay at three different temperatures. At 295 K the slow component is dominant and has the same lifetime as the f–f (b) decay. It is this lifetime that is reported in figure 5 and used for the fitting procedure. The fast component of the f–d (B) decay becomes more visible when the temperature is lowered. The time constant for this fast decay is 1.5($\pm$0.3) $\mu$s at 170 K, decreasing to 1($\pm$0.3) $\mu$s at 78 K. In parallel to this fast decay, an initial rise of the corresponding f–f (b) emission with a 0.7($\pm$0.3) $\mu$s characteristic time is observable at 78 K (figure 7). This is further evidence that the emitting states of the f–f (b) and f–d (B) belong to the same $Eu^{2+}$ ions. The combination of the initial fast decay of the f–d emission with its corresponding f–f rise shows that the lowest $4f^65d^1$ level is populated before $^6P_{7/2}$ after excitation in the parity-allowed f–d bands. At higher temperature, the relative amplitude of the initial decay is reduced since the exchange of population needed to achieve thermal equilibrium is reduced. The population exchange to reach equilibrium takes place on a microsecond timescale and is, to the best of our knowledge, the longest observed for $Eu^{2+}$ in an inorganic crystal. To reach a

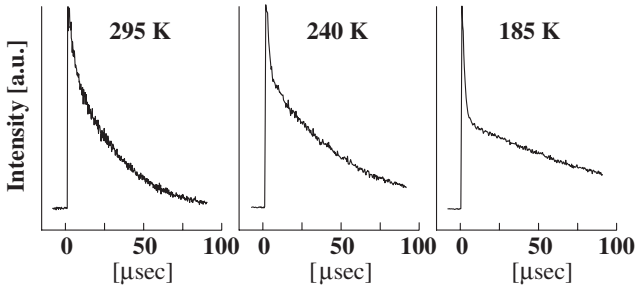


**Figure 6.** Time decay profiles at 295, 240 and 185 K for the inter-configurational f–d (B) emission band in $Ba_2Mg_3F_{10}$:Eu (0.2%) detected at 23 550 $cm^{-1}$ (excitation: 37 594 $cm^{-1}$).

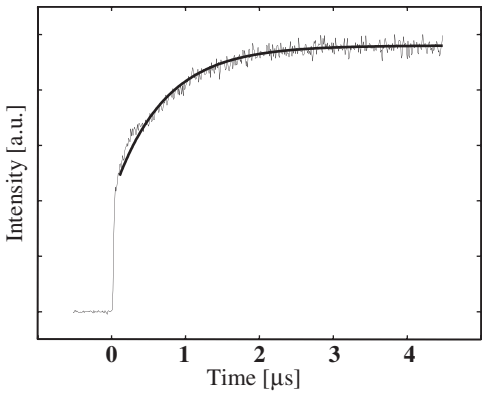


**Figure 7.** Time evolution of the f–f (b) emission in $Ba_2Mg_3F_{10}:Eu^{2+}$ (0.2%). The thick curve indicates the result of a fit with a 0.7 $\mu$s rise time (see text). ($T = 78$ K, detection: 27 784 $cm^{-1}$).

dynamical equilibrium, the ratio between the forward and backward transition rates is related to the energy difference and to the temperature. At 78 K and assuming identical degeneracy for both levels, a 450 $cm^{-1}$ energy difference yields a rate ratio equal to 0.89, which is in agreement with the 0.7($\pm$0.5) ratio experimentally observed. This rather long equilibration time is responsible for the slightly longer f–f (b) emission decay compared to the corresponding f–d (B) decay (figure 5). For the Eu1 emitting centre, this discrepancy is less marked since the equilibration time is much faster.

Using the energy difference $\Delta E$ between the lowest $4f^65d^1$ level and $^6P_{7/2}$ levels, the f–d Stokes shifts for both $Eu^{2+}$ types are estimated and given in table 3. Eu1 presents a 4.4 fold larger Stokes shift. This corresponds to a stronger vibronic coupling which is explained by the Eu1 cluster geometry. In the Eu1 cluster, two fluoride ions are at a much shorter distance (260 pm) compared to the shortest Eu–F distance (272 pm) in the Eu2 cluster. A shorter Eu–F distance thus allows a stronger coupling between the $4f^65d^1$ level of $Eu^{2+}$ and the lattice vibrations. The Eu1 large Stokes-shift indicates an important rearrangement of the $4f^65d^1$ excited state geometry. Such a rearrangement causes, at least partly, the long extra-configurational equilibration time of this excited state.

## 4. Conclusion

The luminescence properties of $Eu^{2+}$ ions introduced in the $Ba_2Mg_3F_{10}$ host were investigated. The emission spectrum consists of two broad f–d bands and two f–f quartets. The assignment

of the different f–f and f–d emissions was made using their individual excitation spectra and lifetime decay. Each line belonging to a given f–f quartet has the same lifetime, and each quartet lifetime is in close agreement with the lifetime of one of the f–d bands. This indicates an equilibrium between the f–f and f–d emitting states on a given $Eu^{2+}$ centre. Lowering the temperature increases the f–f emission intensity at the expense of the f–d transition; the lowest $4f^65d^1$ state is thus at higher energy than the $^6P_{7/2}$ one.

A three-level model was used to fit the temperature dependence of the decay time for the two types of emitting $Eu^{2+}$. This leads to an estimate of the energy difference between the lowest $^6P_{7/2}$ component and the lowest $4f^65d^1$ level. Based on these fits, the two energy differences (600, 450 $cm^{-1}$) and the corresponding Stokes shifts (1700, 7500 $cm^{-1}$) were calculated.

At low temperature, one $Eu^{2+}$ centre shows an f–f decay profile with two components. The slow component corresponds to the emission decay after the system has reached equilibrium. The additional fast decay component is directly related to an initial rise of the corresponding f–d emission. This demonstrates that the lowest $4f^65d^1$ level is populated before the $^6P_{7/2}$ level after excitation and that the exchange of population needed to achieve thermal equilibrium takes place on a microsecond timescale.

Based on the $Ba_2Mg_3F_{10}$ crystal structure, the second rank crystal field parameters and their influence on the $^6P_{7/2}$ exited states of $Eu^{2+}$ have been modelled. The resulting good agreement between the experimental and calculated energy levels allowed the assignment of each f–f emission to its corresponding $Eu^{2+}$ centre. Each centre is formed by substitution at a given $Ba^{2+}$ site in the crystal structure.

## Acknowledgments

This work was supported by the Swiss Priority Program Optics 2 and the Swiss National Science Foundation.

We are indebted to Professor M F Reid (University of Canterbury, New Zealand) for allowing us to use his f-shell programs.

## References

[1] Kaminskii A A 1990 *Laser Crystals* (*Springer Series in Optical Sciences* vol 14) (Berlin: Springer)
[2] Kobayasi T, Mroczkowski S, Owen J F and Brixner L H 1980 *J. Lumin.* **21** 247
[3] Jaaniso R and Bill H 1991 *Europhys. Lett.* **16** 569
[4] Bill H, Jaaniso R, Hageman H, Lovy D, Monnier A and Schnieper M 1995 *Opt. Eng.* **34** 2333
[5] Nicollin D and Bill H 1978 *J. Phys. C: Solid State Phys.* **11** 4803
Nicollin D and Bill H 1976 *Solid State Commun.* **20** 135
[6] Fouassier C, Latourette B, Portier J and Hagenmuller P 1976 *Mater. Res. Bull.* **11** 933
[7] Rubio J 1991 *J. Phys. Chem. Solids* **52** 101
[8] Wegh R T, Donker H, Oskam K D and Meijerink A 1999 *Science* **283** 664
[9] van Pieterson L, Reid M F, Wegh R T, Soverna S and Meijerink A 2002 *Phys. Rev.* B **65** 045113
[10] Dorenbos P 2000 *J. Lumin.* **91** 91
[11] Dieke G H 1968 *Spectra and Energy Levels of Rare Earth Ions in Crystals* (New York: Wiley)
[12] Gingl F 1997 *Z. Anorg. Allg. Chem.* **623** 705
[13] Rey J M, Bill H, Lovy D and Hagemann H 1998 *J. Alloys Compounds* **274** 164
[14] Rey J M, Bill H, Lovy D and Hagemann H 1998 *J. Alloys Compounds* **268** 60
[15] Downer M C, Cordero-Montalvo C D and Crosswhite H 1983 *Phys. Rev.* B **28** 4931
[16] Kubel F, Hagemann H and Bill H 1999 *Z. Kristallogr.* **214** 139
[17] Feofilov P P and Tolstoi M N 1962 *Opt. Spectrosc.* **13** 164
[18] Meijerink A 1993 *J. Lumin.* **55** 125
[19] Meijerink A, Nuyten J and Blasse G 1989 *J. Lumin.* **44** 19